

The SMC SNR 1E0102.2-7219 as a Calibration Standard for X-ray Astronomy in the 0.3-2.5 keV Bandpass

Paul P. Plucinsky^a, Frank Haberl^b, Daniel Dewey^c, Andrew P. Beardmore^d, Joseph M. DePasquale^a, Olivier Godet^d, Victoria Grinberg^b, Eric D. Miller^c, A.M.T. Pollock^e, Steve Sembay^d, Randall K. Smith^g

^aHarvard-Smithsonian Center for Astrophysics, 60 Garden St., Cambridge, MA, USA 02138

^bMax-Planck-Institut für Extraterrestrische Physik, Giessenbachstraße, 85748 Garching, Germany

^cMIT Kavli Institute for Astrophysics and Space Research, Cambridge, MA 02139

^dDepartment of Physics and Astronomy, University of Leicester, Leicester LE1 7RH

^eEuropean Space Astronomy Centre, Apartado 78, Villanueva del Canada, 28691 Madrid, Spain

^gCode 662 NASA Goddard Space Flight Center, Greenbelt, MD, USA 20771

ABSTRACT

The flight calibration of the spectral response of CCD instruments below 1.5 keV is difficult in general because of the lack of strong lines in the on-board calibration sources typically available. We have been using 1E 0102.2-7219 the brightest supernova remnant in the Small Magellanic Cloud, to evaluate the response models of the ACIS CCDs on the Chandra X-ray Observatory (CXO), the EPIC CCDs on the XMM-Newton Observatory, the XIS CCDs on the *Suzaku* Observatory, and the XRT CCD on the *Swift* Observatory. E0102 has strong lines of O, Ne, and Mg below 1.5 keV and little or no Fe emission to complicate the spectrum. The spectrum of E0102 has been well characterized using high-resolution grating instruments, namely the XMM-Newton RGS and the CXO HETG, through which a consistent spectral model has been developed that can then be used to fit the lower-resolution CCD spectra. Fits with this model are sensitive to any problems with the gain calibration and the spectral redistribution model of the CCD instruments. We have also used the measured intensities of the lines to investigate the consistency of the effective area models for the various instruments around the bright O (~ 570 eV and ~ 654 eV) and Ne (~ 910 eV and ~ 1022 eV) lines. We find that the measured fluxes of the O VII triplet, the O VIII Ly α line, the Ne IX triplet, and the Ne X Ly α line generally agree to within $\pm 10\%$ for all instruments, with 28 of our 32 fitted normalizations within $\pm 10\%$ of the RGS-determined value. The maximum discrepancies, computed as the percentage difference between the lowest and highest normalization for any instrument pair, are 23% for the O VII triplet, 24% for the O VIII Ly α line, 13% for the Ne IX triplet, and 19% for the Ne X Ly α line. If only the CXO and XMM are compared, the maximum discrepancies are 22% for the O VII triplet, 16% for the O VIII Ly α line, 4% for the Ne IX triplet, and 12% for the Ne X Ly α line.

Keywords: Chandra X-ray Observatory, XMM-Newton, Suzaku, Swift, ACIS, EPIC, RGS, HETG, XIS, XRT, charge-coupled devices (CCDs), X-ray detectors, X-ray spectroscopy

1. INTRODUCTION

This paper reports the progress of a working group within the *International Astronomical Consortium for High Energy Calibration* (IACHEC) to develop a calibration standard for X-ray astronomy in the bandpass from 0.3 to 2.5 keV. A brief introduction to the IACHEC organization, its objectives and meetings, may be found at the web page <http://www.iachec.org/>. Our working group was tasked with selecting celestial sources with line-rich spectra in the 0.3-2.5 keV bandpass which would be suitable cross-calibration targets for the current generation of

Further author information: (Send correspondence to Paul Plucinsky)
Paul Plucinsky.: E-mail: plucinsky@cfa.harvard.edu

X-ray observatories. The desire for strong lines in this bandpass stems from the fact that the quantum efficiency and spectral resolution of the current CCD-based instruments is changing rapidly from 0.3 to 1.5 keV and also significantly around the Si K edge, but the on-board calibration sources currently in use typically have strong lines at only two energies, 1.5 keV (Al K α) and 5.9 keV (Mn K α). The only option available to the current generation of flight instruments to calibrate any time variable response is to use celestial sources. The missions which have been represented in this work are the *Chandra X-ray Observatory*^{1,2} (CXO), the *X-ray Multimirror Mission*³ (XMM-Newton), the *ASTRO-E2 Observatory (Suzaku)*, and the *Swift Gamma-ray Burst Mission*. Data from the following instruments have been included in this analysis: the *High-Energy Transmission Grating* (HETG) and the *Advanced CCD Imaging Spectrometer*⁴⁻⁶ (ACIS) on the CXO, the *Reflection Gratings Spectrometers*⁷ (RGS), the *European Photon Imaging Camera* (EPIC) *Metal-Oxide Semiconductor*⁸ (MOS) CCDs and the EPIC p-n junction⁹ (pn) CCDs on XMM-Newton, the *X-ray Imaging Spectrometer* (XIS) on *Suzaku*, and the *X-ray Telescope*^{10,11} (XRT) on *Swift*.

Suitable calibration targets would need to possess the following qualities. The source would need to be constant in time, to have a simple spectrum defined by a few bright lines with a minimum of line-blending, and to be extended so that “pileup” effects in the CCDs are minimized but not so extended that the off-axis response of the telescope dominates the uncertainties in the response. Our working group focused on supernova remnants (SNRs) with thermal spectra and without a central source such as a pulsar, as the class of source which had the greatest likelihood of satisfying these criteria. We narrowed our list to the Galactic SNR Cas-A, the Large Magellanic Cloud remnant N132D and the Small Magellanic Cloud remnant 1E 0102.2-7219. We discarded Cas-A since it is a relatively young (~ 350 yr) SNR with significant brightness fluctuations in the X-ray, radio, and optical over the past three decades, it contains a faint (but apparently constant) central source, and it is relatively large (radius ~ 3.5 arcminutes). We discarded N132D because it has a complicated, irregular morphology in the X-rays and its spectrum shows strong, complex Fe emission. We therefore settled on 1E 0102.2-7219 as the most suitable source given its relatively uniform morphology, small size (radius ~ 0.4 arcminutes), and comparatively simple X-ray spectrum.

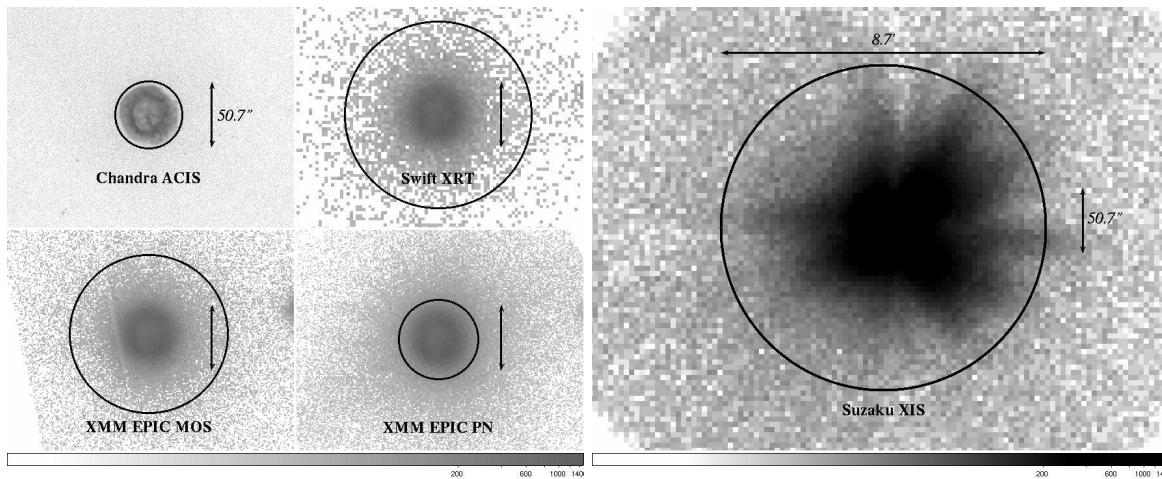


Figure 1. Images of E0102 from ACIS S3 (top left), MOS (bottom left), XRT (middle top), pn (middle bottom), and XIS (right). The black circles indicate the extraction regions used for the spectral analysis. The high angular resolution of the CXO’s mirrors are evident in the structure resolved in the SNR and the small extraction region.

The SNR 1E 0102.2-7219 (hereafter E0102) was discovered by the *Einstein Observatory*.¹² It is the brightest SNR in X-rays in the *Small Magellanic Cloud* (SMC). E0102 has been extensively imaged by CXO^{13,14} and XMM-Newton.¹⁵ Figure 1 shows an image of E0102 with the relevant spectral extraction region for each of the instruments included in this analysis. E0102 is classified as an “O-rich” SNR and has an estimated age of $\sim 1,000$ yr. The source diameter is small enough such that a high resolution spectrum may be acquired with the HETG on the CXO and the RGS on XMM-Newton. The HETG spectrum¹⁶ and the RGS spectrum¹⁷ both show strong lines of O, Ne, and Mg with little or no Fe. E0102’s spectrum is relatively simple compared to a typical SNR spectrum. Figure 2 displays the RGS spectrum from E0102. The strong, well-separated lines in the

energy range 0.5 to 1.5 keV make this source a useful target for calibration observations. The source is extended enough to reduce the effects of photon pileup, which distorts a spectrum. Although moderate pileup is expected in all the non-grating instruments when observed in modes with relatively long frame times. The source is also bright enough to provide a large number of counts in a relatively short observation.

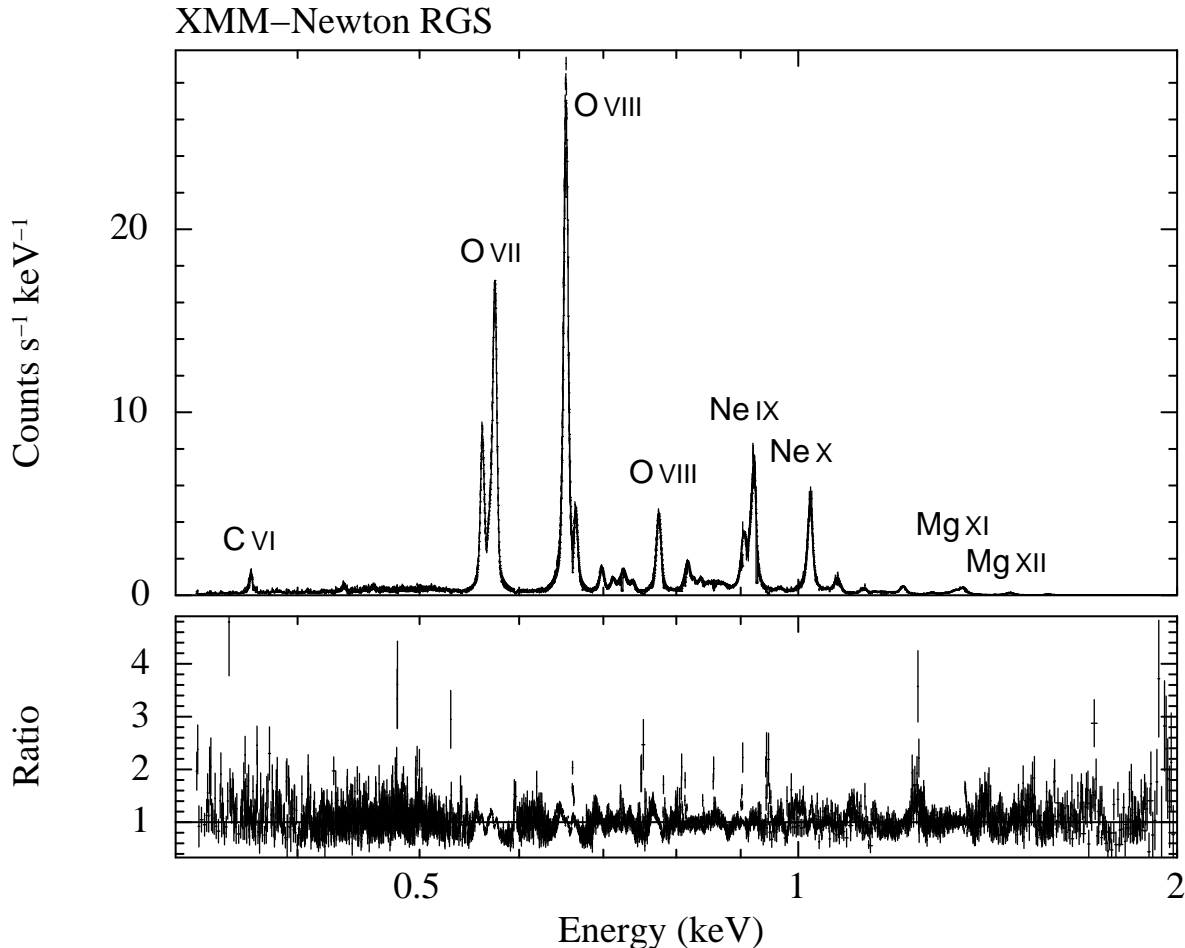


Figure 2. RGS1/2 spectrum of E0102 from a combination of 23 observations. Note the bright lines of O, Ne, and Mg.

2. CONSTRUCTION OF THE MODEL

Our objective was to develop a model which would be useful in calibrating and comparing the response of the CCD instruments; therefore, the model presented here is of limited value for understanding E0102 as a SNR. Our approach was to rely upon the high-resolution spectral data from the RGS and HETG to identify and characterize the bright lines and the continuum in the energy range from 0.3-2.0 keV and the moderate-spectral resolution data from the MOS and pn to characterize the lines and continuum above 2.0 keV. Since our objective is calibration, we decided against using any of the available plasma emission models for several reasons. First, the CXO results on E0102^{13, 14, 16} have shown there are significant spectral variations with position in the SNR, implying that the plasma conditions are varying throughout the remnant. Since the other missions considered here have poorer angular resolution than the CXO, the emission from these regions is mixed such that the unambiguous interpretation of the fitted parameters of a plasma emission model is difficult if not impossible. Second, the available parameter space in the more complex codes is large, making it difficult to converge on a single best fit which represents the spectrum. We therefore decided to construct a simple, empirical model based on interstellar absorption components, Gaussians for the line emission, and continuum components which would be appropriate for our limited calibration objectives.

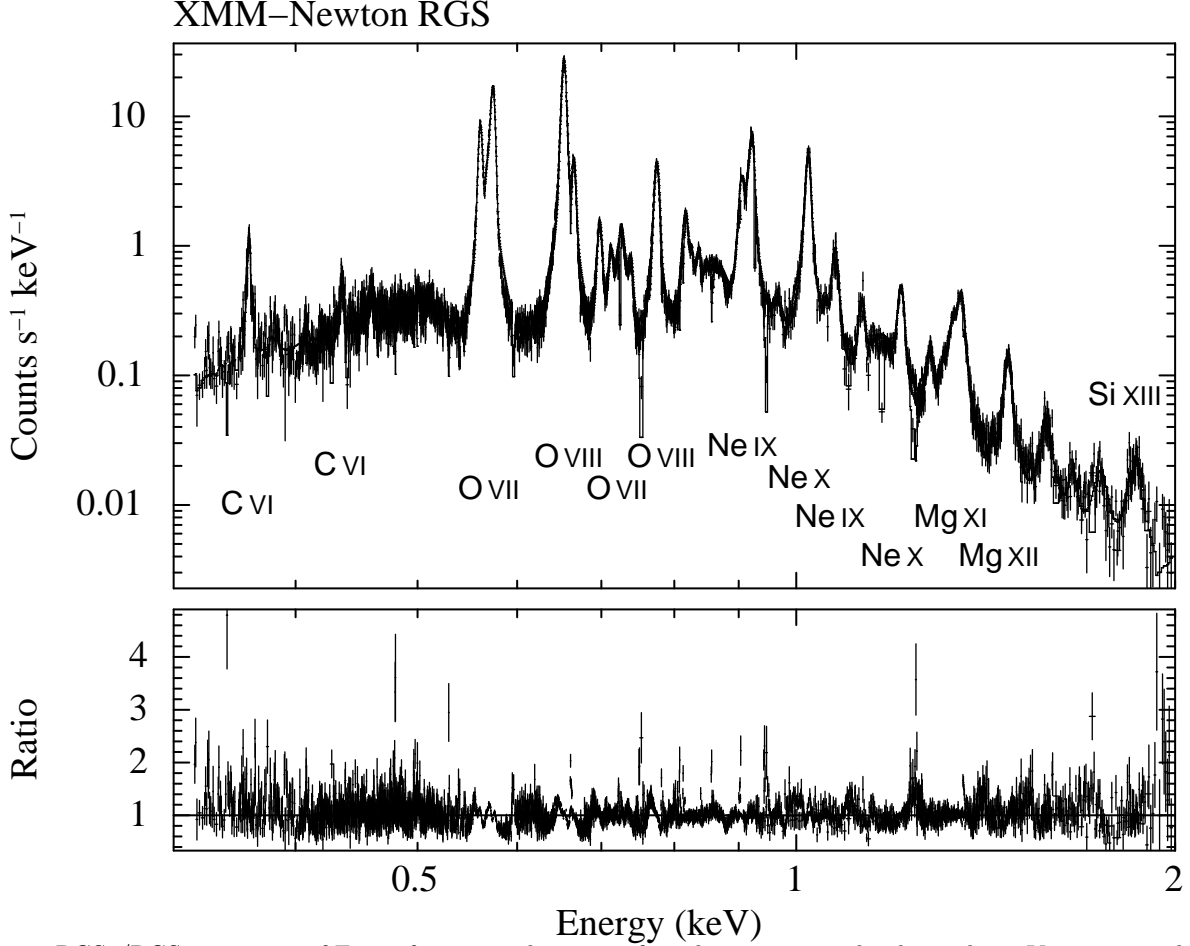


Figure 3. RGS1/RGS2 spectrum of E0102 from a combination of 23 observations with a logarithmic Y axis to emphasize the continuum and the weakest lines.

We assumed a two component absorption model using the `tbabs`¹⁸ model in `XSPEC`. The first component was held fixed at $5.36 \times 10^{20} \text{ cm}^{-2}$ to account for absorption in the Galaxy. The second component was allowed to vary in total column, but with the abundances fixed to the lower abundances of the SMC.^{19–21} We modeled the continuum using a modified version of the `APEC` plasma emission model²² called the ‘‘No-Line’’ model. This model excludes all line emission, while retaining all continuum processes including bremsstrahlung, radiative recombination continua (RRC), and the two-photon continuum from hydrogenic and helium-like ions (from the strictly forbidden $^2S_{1/2}2s \rightarrow \text{gnd}$ and $^1S_01s2s \rightarrow \text{gnd}$ transitions, respectively). Although the bremsstrahlung continuum dominates the X-ray spectrum in most bands and at most temperatures, the RRCs can produce observable edges while the two-photon emission creates ‘bumps’ in specific energy ranges. The ‘‘No-Line’’ model assumes collisional equilibrium and so may overestimate the RRC edges in an ionizing plasma or have the wrong total flux in some of the two-photon continua. However, the available data did not justify the use of a more complex model, while the simpler bremsstrahlung-only model showed residuals in the RGS spectra that were strongly suggestive of RRC edges. The RGS data were adequately fit by a single continuum component, but the HETG, MOS, and pn data showed an excess at energies above 2.0 keV. We therefore added a second continuum component to account for this emission.

The lines were modeled as simple Gaussians in `XSPEC`. The lines were identified in the RGS and HETG data in a hierarchical manner, starting with the brightest lines and working down to the fainter lines. We have used the `ATOMDB` v1.3.1²³ database to identify the transitions which produce the observed lines. The RGS spectrum from 23 observations totaling 708/680 ks for RGS1/RGS2 is shown in Figure 2 with a linear Y axis to emphasize

the brightest lines. The spectrum is dominated by the O VII triplet at 560-574 eV, the O VIII Ly α line at 654 eV, the Ne IX triplet at 905-922 eV, and the Ne X Ly α at 1022 eV. This figure demonstrates the lack of strong Fe emission in the spectrum of E0102. The identification of the lines obviously becomes more difficult as the lines become weaker. Figure 3 shows the same spectrum as in Figure 2 but with a logarithmic axis. In this figure, one is able to see the weaker lines more clearly and also the shape of the continuum. Lines were added to the spectrum at the known energies for the dominant elements, C, N, O, Ne, Mg, Si, S, and Fe and the resulting decrease in the reduced χ^2 value was evaluated to determine if the addition of the line was significant. The list of lines identified in the RGS and HETG data were checked for consistency. The identified lines were compared against representative spectra from the `vpshock` model (with lines) to ensure that no strong lines were missed. Figure 4 shows the comparison of our hybrid model of continuum and lines to a representative spectrum from the `vpshock` model.

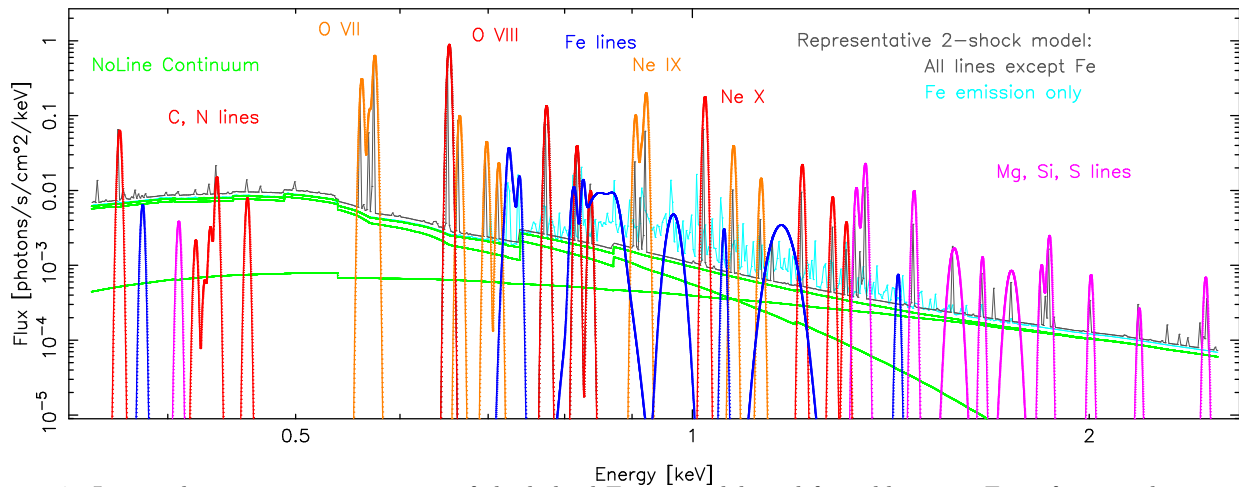


Figure 4. Line and continuum components of the hybrid E0102 model used for calibration. For reference, the emission predicted by a simple two-`vpshock` model, scaled and summed with our continuum model, is shown. The calibration model clearly includes all expected bright lines as well as additional flux that may correspond to Fe emission from E0102. For a color version of this figure see the on-line version.

In this manner a list of lines in the 0.3-2.0 keV bandpass was developed based upon the RGS and HETG data. In addition, the temperature and normalization were determined for the low-temperature APEC ‘‘No-Line’’ continuum component. These model components were then frozen and the model compared to the pn, MOS, and XIS data. Weak lines above 2.0 keV were evident in the pn, MOS, and XIS data and also what appeared to be an additional continuum component above 2.0 keV. Several lines were added above 2.0 keV and a high-temperature continuum component with $kT \sim 1.7$ keV was added. Once the model components above 2.0 keV had been determined, the RGS data were re-fit with components above 2.0 keV frozen to these values and the final values for the SMC N_H and the low-temperature continuum were determined. In practice, this was an iterative process which required several iterations in fitting the RGS and MOS/pn/XIS data. Once the absorption and continuum components were determined, the parameters for those components were frozen and the final parameters for the line emission were determined from the RGS data. We included 52 lines in the final model and these lines are described in Table 1. When fitting the RGS data, the line energies were allowed to vary by up to 1.0 eV from the expected energy to account for the shifts when an extended source is observed by the RGS. Shifts of less than 1.0 eV are too small to be significant when fitting the CCD instrument data. The line widths were also allowed to vary. In most cases the line widths are small but non-zero, consistent with the Doppler widths seen in the RGS¹⁷ and HETG¹⁶, $\sigma_E \approx 0.003 \times E$; but in a few cases noted in the table the widths are larger than this value. This is mostly like due to weak, nearby lines which our model has ignored. We do not have an identification for the line-like feature at 1.4317 keV.

As noted above, the identification of the lines becomes less certain as the line fluxes get weaker. Our primary purpose is to characterize the flux in the bright lines of O, Ne, and Mg. Any identification of a line with flux less

than 1.0×10^{-4} photons $\text{cm}^{-2} \text{s}^{-1}$ in Table 1 should be considered tentative. The Fe lines in Table 1 warrant special discussion. There are nine Fe lines included in our model from different ions. We have not verified the self-consistency of the Fe lines included in this model. We anticipate that we will work on this in the near future. Of particular note is the Fe XIX line at 917 eV with zero flux. We went through several iterations of the model with this line included and excluded. Unfortunately this line is only 2 eV away from the Ne IX Intercombination line at 915 eV and neither the RGS nor the HETG have the resolution to characterize the emission in this region. We have decided to attribute all the flux in this region to the Ne IX Intercombination line but have retained the Fe XIX for future investigations. It is possible that some of the emission which we have identified as Fe emission is due to other elements. For our calibration objective this is not important because all of the Fe lines are weak and they do not have a significant effect on the fitted parameters of the bright lines of O, Ne, and Mg. We hope that future instruments will have the resolution and sensitivity to uniquely identify the weak lines in the E0102 spectrum.

Table 1. Spectral Lines Included in the E0102 Reference Model (v1.9)

Line ID	E (keV) ^a	λ (Å) ^a	Flux ^b	Line ID	E (keV) ^a	λ (Å) ^a	Flux ^b
C VI Ly α	0.3675	33.737	175.2	Ne IX i	0.9148	13.553	249.6
Fe XXIV	0.3826	32.405	18.4	Fe XIX	0.9172	13.517	0.0
S XIV	0.4075	30.425	11.8	Ne IX r	0.922	13.447	1380.5
N VI f	0.4198	29.534	6.8	Fe XX	0.9668 ^c	12.824	120.5
N VI i	0.4264	29.076	2.0	Ne X Ly α	1.0217	12.135	1378.3
N VI r	0.4307	28.786	10.5	Fe XXIII	1.0564	11.736	24.2
C VI Ly β	0.4356	28.462	49.5	Ne IX He β	1.074	11.544	320.7
C VI Ly γ	0.4594	26.988	27.3	Ne IX He γ	1.127	11.001	123.1
O VII f	0.561	22.1	1313.2	Fe XXIV	1.168 ^c	10.615	173.5
O VII i	0.5686	21.805	494.4	Ne X Ly β	1.211	10.238	202.2
O VII r	0.5739	21.603	2744.7	Ne X Ly γ	1.277	9.709	78.5
O VIII Ly α	0.6536	18.969	4393.3	Ne X Ly δ	1.308	9.478	37.1
O VII He β	0.6656	18.627	500.9	Mg XI f	1.3311	9.314	108.7
O VII He γ	0.6978	17.767	236.1	Mg XI i	1.3431	9.231	27.5
O VII He δ	0.7127	17.396	124.9	Mg XI r	1.3522	9.169	231.0
Fe XVII	0.7252	17.096	130.9	? ?	1.4317	8.659	8.1
Fe XVII	0.7271 ^c	17.051	165.9	Mg XII Ly α	1.4721	8.422	110.2
Fe XVII	0.7389	16.779	82.3	Mg XI He β	1.579 ^c	7.852	50.6
O VIII Ly β	0.7746	16.006	788.6	Mg XI He γ	1.659	7.473	16.0
Fe XVII	0.8124 ^c	15.261	90.5	Mg XII Ly β	1.745 ^c	7.105	29.7
O VIII Ly γ	0.817	15.175	243.1	Si XIII f	1.8395	6.74	13.8
Fe XVII	0.8258	15.013	65.1	Si XIII i	1.8538	6.688	3.4
O VIII Ly δ	0.8365	14.821	62.7	Si XIII r	1.865	6.647	34.6
Fe XVIII	0.8503 ^c	14.581	407.3	Si XIV Ly α	2.0052	6.183	11.2
Fe XVIII	0.8726 ^c	14.208	89.6	Si XIII He β	2.1818	5.682	4.3
Ne IX f	0.9051	13.698	690.2	S XV f,i,r	2.45	5.06	12.7

^a Theoretical rest energies; wavelengths are hc/E .

^b Observed flux in 10^{-6} photons $\text{cm}^{-2} \text{s}^{-1}$

^c This line is broader than the nominal width, see text

The number of free parameters needed to be significantly reduced before fitting the CCD data in order to reduce the possible parameter space. In our fits, we have frozen the line energies and widths, the SMC N_{H} , and the low-temperature APEC ‘‘No-Line’’ continuum to the RGS-determined values. The high-temperature APEC ‘‘No-Line’’ component was frozen at the values determined from the pn and MOS. The fixed absorption and continuum components are listed in Table 2. Since the CCD instruments lack the spectral resolution to resolve lines which are as close to each other as the ones in the O VII triplet and the Ne IX triplet, we treated nearby

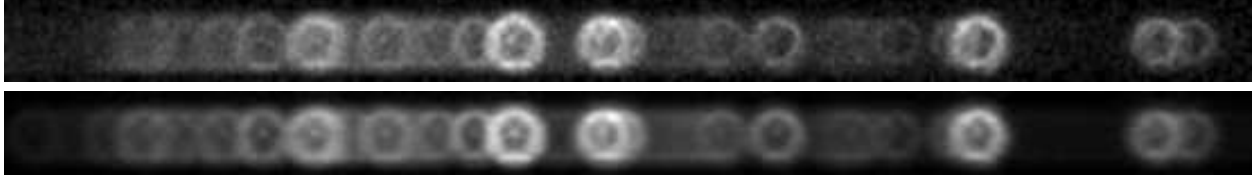


Figure 5. Images of E0102 MEG-dispersed data (top) and model (bottom). The four MEG dispersed images (± 1 orders from two epochs) have been combined and displayed in the range from 4.6\AA to 23\AA (2.7–0.54 keV), clearly showing bright rings of line emission for many lines. The simulated spectral image, below, is based on the nominal hybrid model.

lines from the same ion as a “line complex” by constraining the ratios of the line normalizations to be those determined by the RGS and by constraining the line energies to the known separations. In practice, we would typically link the normalization and energy of the Forbidden and Intercombination lines of the triplet to the Resonance line (except for O VII for which we linked the other lines to the Forbidden line). Since we also usually freeze the energies of the lines, this means that the three lines in the triplet would have only one free parameter, the normalization of the Resonance line. We have constructed the model in XSPEC such that it would be easy to vary the energy of the Resonance line in the triplet (and hence also the Forbidden and Intercombination) to examine the gain calibration of a detector at these energies. Our philosophy is to treat nearby lines as a complex which can adjust together in normalization and energy. In this paper, we focus on adjusting the normalization of the line complexes only. Since most of the power in the spectrum is in the bright line complexes, we froze all the normalizations of the weaker lines. The only normalizations which we allowed to vary were the O VII For, O VIII Ly α line, the Ne IX Res, and the Ne X Ly α line normalizations. In addition, we found it useful to introduce a constant scaling factor of the entire model to account for the fact that the extraction regions for the various instruments were not identical. Finally, some of the instruments found it useful to allow for a global gain shift. In this manner, we restricted a model with more than 200 parameters to have only 5 or 7 free parameters in our fits. The final version of this model in the XSPEC .xcm file format is available at the web page: ‘<http://cxc.harvard.edu/twiki/bin/view.cgi/SnrE0102/FinalModel>’.

Table 2. Fixed Absorption and Continuum Components

Galactic absorption	$N_{\text{H}} = 5.36 \times 10^{20} \text{ cm}^{-2}$
SMC absorption	$N_{\text{H}} = 5.76 \times 10^{20} \text{ cm}^{-2}$
APEC ‘No-Line’ temperature #1	kT=0.164 keV
APEC ‘No-Line’ normalization #1	$3.48 \times 10^{-2} \text{ cm}^{-5}$
APEC ‘No-Line’ temperature #2	kT=1.736 keV
APEC ‘No-Line’ normalization #2	$1.85 \times 10^{-3} \text{ cm}^{-5}$

3. OBSERVATIONS

E0102 is routinely observed by the CXO, XMM-Newton and *Suzaku*, as a calibration target to monitor the response at energies below 1.5 keV. For this paper, we have selected a subset of these observations for each instrument since E0102 has been observed in different modes for each instrument. We have selected data from the instrument mode for which we are the most confident in the calibration. We now describe the data processing and calibration issues for each instrument individually.

RGS: From all 23 XMM-Newton observations of E0102 between 16 April 2000 and 26 Oct 2007, we extracted spectra from the RGS instruments. For the complete analysis RGS1 and RGS2 were handled separately. The data were processed with XMM-SAS v7.1.0 using `rgsproc` for the extraction of the spectra and the generation of the spectral response files. We used the task `rgscombine` to add up the spectra and response files. This yields a total net exposure of 708080 s for RGS1 and 680290 s for RGS2.

HETG: E0102 was observed with the HETG at two epochs: Sept.–Oct. 1999 and in December of 2002; note that the first epoch is very early in the CXO mission and at a focal plane temperature of -110°C . Analysis of the archive-retrieved data was carried out with TGCat ISIS scripts* that called current CIAO tools. Of note

* <http://space.mit.edu/cxc/analysis/tgcat/>

in the analyses: the origin was set at the bright inner spot of the Q-stroke feature; zeroth-order radius was 60 pixels; events were extracted from widths of ± 60 pixels (± 0.0096 in `tg_d`); and order sorting values of 0.25 and 0.20 were used for the first and second epochs, respectively.

The HETG view of E0102 is presented by the first epoch observations.¹⁶ Because of the extended nature of E0102, non-standard analysis methods are needed²⁴ to get information from the 2D dispersed spectral images. Here, “Event2D” software[†] is used to take the E0102 hybrid spectral model, the CIAO-generated `arf`, and E0102 spectral images to create a Monte Carlo simulation of each observation-grating-order data set. Figure 5 shows the data and simulated model for the combined MEG data sets. The second epoch data and model were compared using the number of counts in six wavelength ranges covering the 0.54 keV to 1.58 keV high-counts range of the MEG plus and minus first orders. This crude binning provides for a quantitative comparison at the level of the CCD analyses. The resulting 12 ratios of data/model and their errors were then used to determine the frozen χ^2 and then the best fit values for the 5 free model parameters; these results are given in the Tables 4 and 5.

MOS: The EPIC MOS data were taken from two observations in XMM revolution 0065 and 0247. Both MOS1 and MOS2 cameras were in Large Window mode (central CCD has 300×300 pixels with a frame time of 0.9s) with the thin filter in each observation. The source region was chosen to be a circle of radius $60''$ centered on the remnant. A background region of the same size was selected within the same central CCD. Response files were calculated using the XMM Science Analysis Software (SAS) task `rmfgen` and `arfgen`. As the source is not a point source a map of the remnant in detector coordinates was used as an input image to `arfgen` so that the calculated `arf` is weighted by the differential vignetting across the remnant.

In the brightest part of the remnant, the observed per-pixel count rate is approximately $0.005 \text{ cts s}^{-1} \text{ pixel}^{-1}$. The 1% pile-up limit for the MOS is $0.0012 \text{ cts s}^{-1} \text{ pixel}^{-1}$ for an extended source in Large Window mode so some moderate pile-up may be expected. We have applied a first order pile-up correction by using the information from the diagonal bi-pixel events in the MOS event files. The details of the pileup correction are documented in the memo XMM-SOC-CAL-TN-0036 available from the ESAC website at:

http://xmm2.esac.esa.int/external/xmm_sw_cal/calib/documentation/index.shtml#EPIC.

The data were then compared against the model for E0102. It was found that a significant improvement in the fit statistic was achieved in both cameras with a small gain shift. The fit statistics including the gain fit parameters are given in Table 4.

pn: Observations of 1E0102 with EPIC pn were performed in full-frame, large window and small window mode using all available filters. To completely avoid pile-up effects we used only data from small window mode. The data were processed with XMM-SAS v7.1.0 without utilizing the most recent up date of the long-term CTI calibration adjustment available with `EPN_CTL0017.CCF` which became public on 12 April 2008. Spectra were extracted using single-pixel events from a circular region around the supernova remnant with a radius of 30 arcsec. Background spectra were extracted from a nearby circular region with the same size. Response files were generated using `rmfgen` and `arfgen`, assuming a point source for PSF corrections.

ACIS: The high angular resolution of the CXO compared to the other observatories is apparent in Figure 1. Unfortunately the bright parts of E0102 are significantly piled-up when ACIS is operated in its full-frame mode with 3.2 s exposures. Also unfortunately, the majority of the observations of E0102 over the mission have been executed in full-frame mode. There have been four subarray observations of E0102, two in node 1 and two in node 0 of the Backside-illuminated (BI) CCD S3. We have selected two OBSIDs from node 1 since the calibration in node 1 is superior to that of node 0. The data were processed with the CXO analysis SW `CIAO` v4.0 and the CXO calibration database `CALDB` v3.4.3. There are several time-dependent effects which the analysis SW attempts to account for.^{25–27} The most important of these is the efficiency correction for the contaminant on the ACIS optical-blocking filter which significantly reduces the efficiency at energies around the O lines. The analysis SW also corrects for the CTI of the BI CCD (S3), including the time-dependence of the gain.

XIS: The XIS observations include 106 ksec of data from XIS1 (the BI device) and 60 ksec of data from XIS0 (one of three FI devices). This represents the longest single observations of E0102 by *Suzaku*. The data were taken shortly after launch on 17 Dec 2005, when the molecular OBF contamination was still relatively low,

[†] http://space.mit.edu/hydra/E2D_demo/e2d_demo.html

and when spaced-row charge injection (SCI) was not yet being used. Normal observing mode was used, and 3x3 and 5x5 event editing mode were combined in the dataset.

The data were processed with v2.0.6.13 of the XIS pipeline. Spectra were extracted from a 4.35 arcmin (6 mm) aperture (the default for a point source), and background spectra were extracted from a surrounding annulus. Response files were produced with the *Suzaku* FTTOOLS `xisrmfgen` (v2007-05-14) and `xissimarfgen` (v2007-07-16). The ARF includes absorption due to OBF contamination, using the contamination parameters as of 2007-12-24.

An additional point source lies 2 arcmin from E0102, well within the spectral extraction region. This X-ray binary (RXJ0103.6-7201) is well-modeled by a power law with spectral index 0.9 plus a thermal `mekal` component with $kT = 0.15$ keV, with a strong correlation between the component normalizations.²⁸ The emission from this source dominates the extracted spectra above 3 keV; below 2 keV, E0102 thermal emission dominates by several orders of magnitude. We have included the source in our spectral modeling, allowing a single normalization to vary due to the observed source variability.

XRT: The *Swift* XRT observations presented here were restricted to Photon Counting mode data taken from 18 Feb 2005 to 22 May 2005 (observation ID numbers 00050050004,5,8,9), which were obtained before a micrometeoroid impact damaged two central columns on the CCD (on 27 May 2005) and before the effects of CTI became more noticeable from Oct 2005 onwards.

The data were processed using the latest release of the *Swift* software tools (version 2.8, release date 2007-12-07). After the standard data screening was applied the final exposure was 24.2ks. We selected grades 0-12 for the spectral comparison. A circular region of radius 70.7 arcseconds was used for the spectral extraction. There is at present no XRT software tool capable of generating extended source ARF files, however the source was positioned near the centre of the CCD during the observations, so the effects of vignetting were negligible, and the extraction region was judged to contain 95 percent of the EEf. The RMF and ARF calibration files used in the spectral fitting were version 011, which will be available in the next calibration release.

Table 3. Observations Used for this Analysis

OBSID	Instrument	DATE	Exposure(s)	Counts (0.5-2.0 keV)	Mode
3828	ACIS-HETG	2002-12-20	137660.0	49600	TE, Faint, 3.2 s framerate
3545	ACIS-S3	2003-08-08	7862.1	55160	TE, 1/4 subarray, 1.1 s framerate
6765	ACIS-S3	2006-03-19	7635.5	50067	TE, 1/4 subarray, 0.8 s framerate
0412980301	pn	2007-10-26	25690.7	275397	sm win, 6 ms framerate, med filter
0123110201	MOS1	2000-04-16	16784.5	58007	large win, 0.9 s framerate, thin filter
0123110201	MOS2	2000-04-16	16786.7	56235	large win, 0.9 s framerate, thin filter
0135720601	MOS1	2001-04-14	12547.0	43626	large win, 0.9 s framerate, thin filter
0135720601	MOS2	2001-04-14	12548.9	41575	large win, 0.9 s framerate, thin filter
100044010	XIS0	2005-12-17	60000.0	96948	normal,3x3+5x5, SCI off
100044010	XIS1	2005-12-17	106000.0	342505	normal,3x3+5x5, SCI off
00050050004	XRT	2005-02-18	24200	26254	combination of 4 observations

4. RESULTS

The spectra for each of the CCD instruments were first compared to the RGS-determined model without allowing any of the parameters to vary. The resulting values of the χ^2 are listed in Table 4 in the columns labelled “Norms Frozen”. It was noticed during this comparison that the MOS, ACIS, and XIS spectra showed similar residuals in that the model appeared higher than the data at low energies around the O lines. It was also noticed that a global offset to account for different size extraction regions would help to reconcile the overall normalization of the spectra. The spectra were then fit with 5 free parameters (with the exception of the MOS and XIS fits in which two more parameters were allowed to vary to account for a global gain offset). The five free parameters are the constant factor to multiply each spectrum by and the O VII triplet, O VIII Ly α , Ne IX triplet & Ne X Ly α line normalizations. The fits were done first with the constant factor free. The constant factor was then frozen

and the spectra refit and the 90% confidence limit (CL) on the line normalizations determined. Table 4 lists the χ^2 values for these fits in the columns labelled “Norms Free”. Note that the HETG data were fit in six broad energy bands unlike the CCD instruments. None of the fits are formally acceptable and the quality of the fit around the bright lines varies. The spectral fits with the line normalizations free are displayed in the following figures: Figure 6 shows the ACIS data, Figure 8 shows the MOS data, Figure 9 shows the pn data, Figure 10 shows the XIS data, Figure 11 shows the XRT data. The fit to the ACIS data has a reduced χ^2 of 1.72 and appears to fit the data reasonably well with the largest residuals below 0.5 keV and above 1.5 keV. Therefore, the bright O and Ne lines appear to be well-fitted. The MOS1 data have the lowest reduced χ^2 of 1.57 and the data appear to be well-fitted with some small systematics in the residuals. The MOS2 data are not fit as well with a reduced χ^2 of 1.96. The pn data are fitted with a reduced χ^2 of 3.32 with large residuals on the low-energy side of the O VII triplet. Nevertheless, the O VIII Ly α line, the Ne IX Res line, and the Ne X Ly α line appear to be well-fitted. The XIS1 spectral fit has the worst reduced χ^2 of 6.40 with large residuals below 0.5 keV and above 1.5 keV. But the residuals around the O and Ne lines are relatively small. Finally, the XRT data are fit with a reduced χ^2 of 2.32, with large residuals above 1.5 keV presumably due to pileup.

Table 4. **Fit Statistics for the RGS model before and after the Normalizations are Allowed to Vary**

Instrument	Norms Frozen		Norms Free		Gain Offset(keV)	Gain Slope
	DOF	χ^2	DOF	χ^2		
HETG	12	42.7	7	14.1		
ACIS	253	714.1	249	427.3		
MOS1	318	719.1	315	492.9	-1.41×10^{-3}	1.005
MOS2	315	933.1	312	611.7	-1.38×10^{-3}	1.006
pn	365	1292.5	362	1202.2		
XIS0	228	884.7	228	489.2	-8.82×10^{-03}	1.006
XIS1	228	2747.1	228	1456.9	-7.62×10^{-03}	1.009
XRT	119	352.1	116	269.1		

The fitted line normalizations for the O VII For line, the O VIII Ly α line, the Ne IX Res line, & Ne X Ly α line are listed in Table 5. The first and second rows include the results for the RGS1 and RGS2. Note that the line normalizations are the same but the scale factor is 0.96 for RGS2, indicating that there is a systematic 4% offset between RGS1 and RGS2. The results for the other instruments are then presented in groups of three rows. Within a group of three rows for a given instrument, the first row gives the best-fitted value, the second row gives the 90% CL, and the third row gives the “scaled” value where the best-fitted value has been multiplied by the constant factor. Figure 7 presents the data in Table 5 in a graphical manner. The scaled normalizations for each instrument are compared to the RGS-determined values and the average of all instruments is also plotted. Several patterns are clear in this plot. First, ACIS, XIS, and XRT show the same trend of increasing normalization with energy. The MOS1 and MOS2 agree well with the RGS1, but it should be noted that the MOS quantum efficiency was adjusted in 2007 with the goal of improving the agreement with RGS. If the MOS data are analyzed with the previous quantum efficiency model, the pattern in the normalizations looks similar to ACIS, XIS, and XRT. Finally, the pn data appear to be low relative to the RGS1 by about 5%. In general, the scaled normalizations for all instruments agree with the RGS values with $\pm 10\%$. Specifically, 28 of the 32 normalizations are within $\pm 10\%$ of the RGS1 values. The scaled normalizations agree to within 14% and 19% for the Ne IX Res and Ne X Ly α lines respectively. The agreement is significantly worse for the O lines, 24% for the O VIII Ly α line and 23% for the O VII For line. If only the CXO and XMM-Newton instruments are considered the agreement improves. The scaled normalizations agree to within 4% and 12% for the Ne IX Res and Ne X Ly α lines respectively. The discrepancy at Ne X Ly α appears to be due mostly to the pn, with MOS and ACIS in much better agreement ($\sim 3\%$). Again, the agreement is significantly worse for the O lines, 16% for the O VIII Ly α line and 22% for the O VII For line. The discrepancy at O VII For appears to be due mostly to ACIS, with MOS and pn in much better agreement ($\sim 3\%$).

There are several possible reasons for the magnitude of the disagreement for these line normalizations. First, the effective area for some of the instruments might be incorrect at some of the energies examined in this analysis. This is particularly true for ACIS and the XIS since both those instruments have time-variable contamination

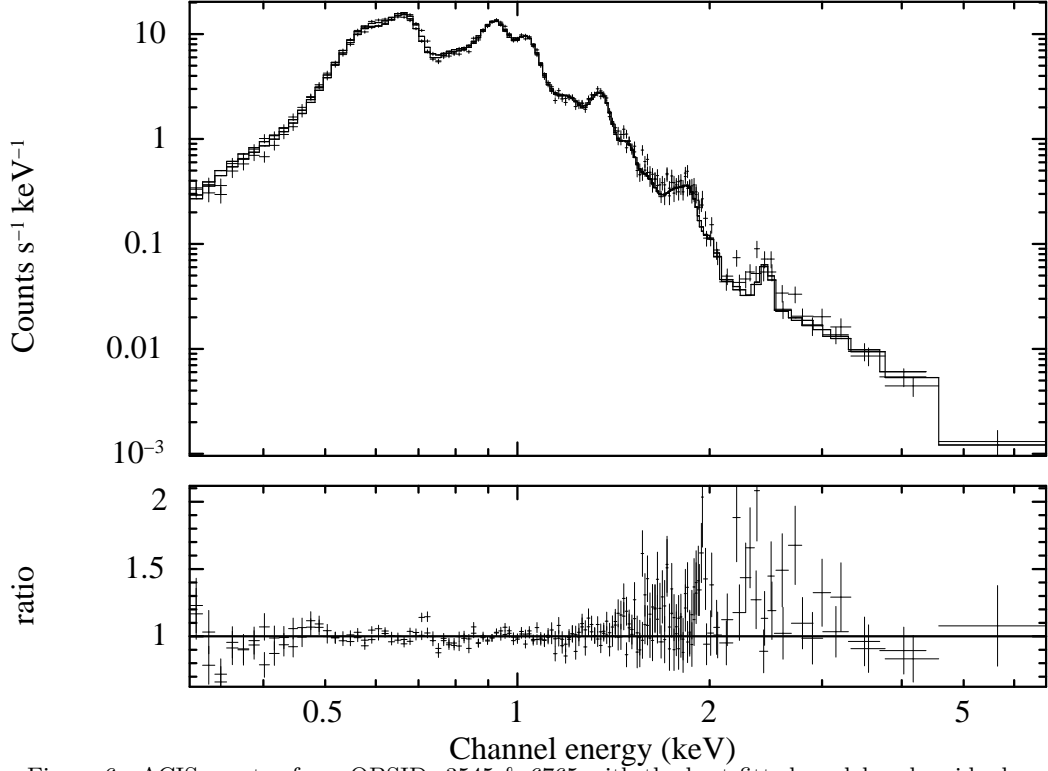


Figure 6. ACIS spectra from OBSIDs 3545 & 6765 with the best-fitted model and residuals.

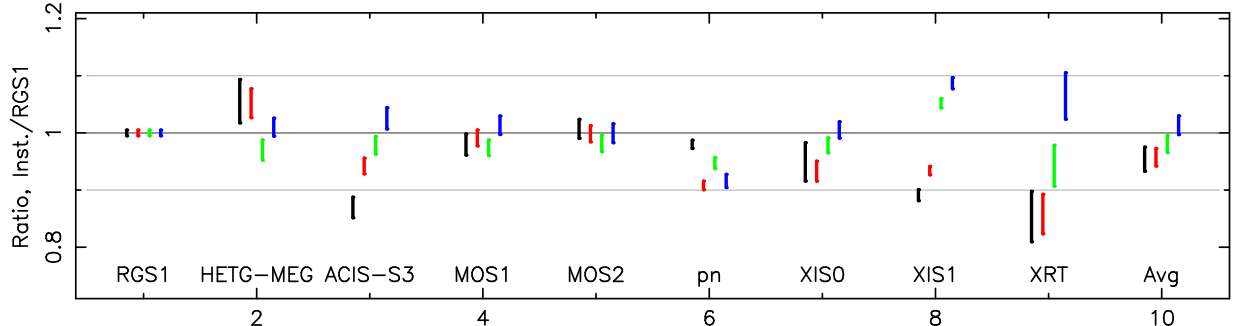


Figure 7. Comparison of the scaled normalizations for each instrument to the RGS values and the average. There are four points for each instrument which are from left to right, O VII, O VIII, Ne IX, & Ne X. The length of the line indicates the 90% CL for the scaled normalization. See the on-line version for a color figure.

layers which significantly affect the effective area at the O lines. Second, the spectral redistribution function for some of the instruments might be incorrect, leading to an incorrect computation of the flux in a line. Third, pileup may be distorting some of the spectra leading to incorrect line normalizations. We will be exploring these possible explanations in the future.

5. CONCLUSIONS

We have use the line-dominated spectrum of the SNR E0102 to test the response models of the ACIS S3, MOS, pn, XIS, and XRT CCDs below 1.5 keV. We have fitted the spectra with the same model in which the continuum and absorption components and the weak lines are held fixed while allowing only the normalizations of four bright lines/line complexes to vary. We have compared the fitted line normalizations of the O VII For line, the O VIII Ly α line, the Ne IX Res line, and Ne X Ly α line to examine the consistency of the effective area

Table 5. Fitted Values for Constant Factor and Line Complex Normalizations

Instrument	Constant	O VII For Norm ($10^{-3}\text{ph cm}^{-2}\text{s}^{-1}$)	O VIII Ly α Norm ($10^{-3}\text{ph cm}^{-2}\text{s}^{-1}$)	Ne IX Res Norm ($10^{-3}\text{ph cm}^{-2}\text{s}^{-1}$)	Ne X Ly α Norm ($10^{-3}\text{ph cm}^{-2}\text{s}^{-1}$)
RGS1	1.00	1.313	4.393	1.381	1.378
RGS2	0.96	1.313	4.393	1.381	1.378
HETG	1.012	1.370	4.567	1.323	1.375
90%CL		[1.320,1.419]	[4.457,4.676]	[1.299,1.347]	[1.354,1.397]
Scaled		1.386	4.622	1.339	1.392
ACIS	1.010	1.130	4.098	1.337	1.400
90%CL		[1.107,1.154]	[4.038,4.158]	[1.316,1.358]	[1.374,1.425]
Scaled		1.141	4.139	1.350	1.414
MOS1	0.993	1.296	4.384	1.354	1.407
90%CL		[1.271,1.320]	[4.323,4.446]	[1.335,1.373]	[1.384,1.429]
Scaled		1.287	4.353	1.345	1.397
MOS2	1.016	1.305	4.318	1.333	1.356
90%CL		[1.280,1.323]	[4.256,4.379]	[1.314,1.353]	[1.333,1.378]
Scaled		1.326	4.387	1.354	1.378
pn	0.942	1.366	4.235	1.388	1.340
90%CL		[1.354,1.378]	[4.200,4.270]	[1.374,1.402]	[1.323,1.356]
Scaled		1.287	3.989	1.307	1.262
XIS0	1.013	1.231	4.047	1.333	1.368
90%CL		[1.187,1.274]	[3.971,4.122]	[1.315,1.351]	[1.348,1.387]
Scaled		1.247	4.100	1.350	1.386
XIS1	1.024	1.142	4.006	1.418	1.463
90%CL		[1.130,1.155]	[3.975,4.038]	[1.407,1.429]	[1.450,1.476]
Scaled		1.169	4.102	1.452	1.498
XRT	0.934	1.206	4.001	1.375	1.551
90%CL		[1.138,1.262]	[3.873,4.198]	[1.340,1.446]	[1.511,1.631]
Scaled		1.126	3.737	1.285	1.448

models for the various instruments in the energy ranges around 570 eV, 654 eV, 915 eV, and 1022 eV. We find that the instruments are in general agreement with 28 of the 32 scaled normalizations within $\pm 10\%$ of the RGS determined values. We find that the scaled line normalizations agree to within 23%, 24%, 13%, & 19% for O VII, O VIII, Ne IX, & Ne X when all instruments are considered. When only CXO and XMM-Newton are considered, we find that the fitted line normalizations agree to within 22%, 16%, 4%, & 12% for O VII, O VIII, Ne IX, & Ne X.

ACKNOWLEDGMENTS

This work was supported by NASA contract NAS8-03060.

We are grateful for the efforts of Marcus Kirsch in organizing and leading the IACHEC which motivated the work which was presented in this paper.

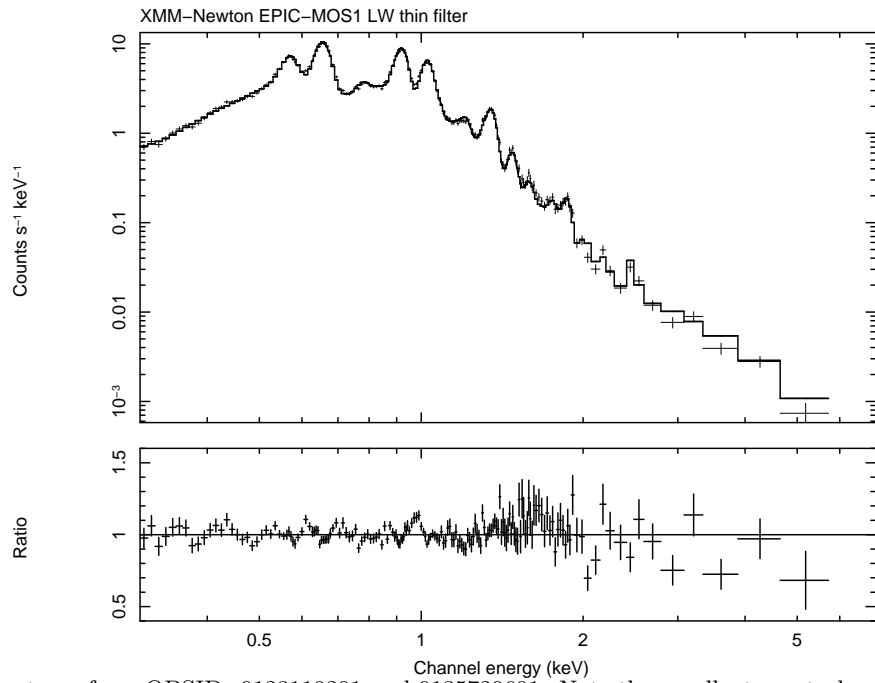


Figure 8. MOS1 spectrum from OBSIDs 0123110201 and 0135720601. Note the excellent spectral resolution of the MOS data.

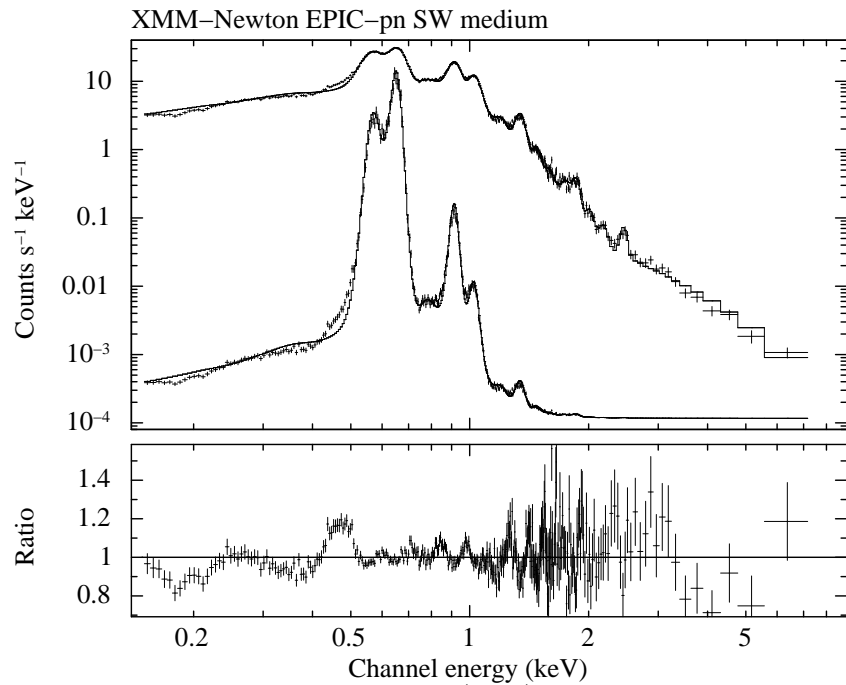


Figure 9. pn spectrum from OBSID0412980301. The second (lower) curve shows the same data but with a linear axis which has been shifted downwards for clarity. Note the high count rate and the pattern in the residuals which might indicate an issue with the spectral redistribution function.

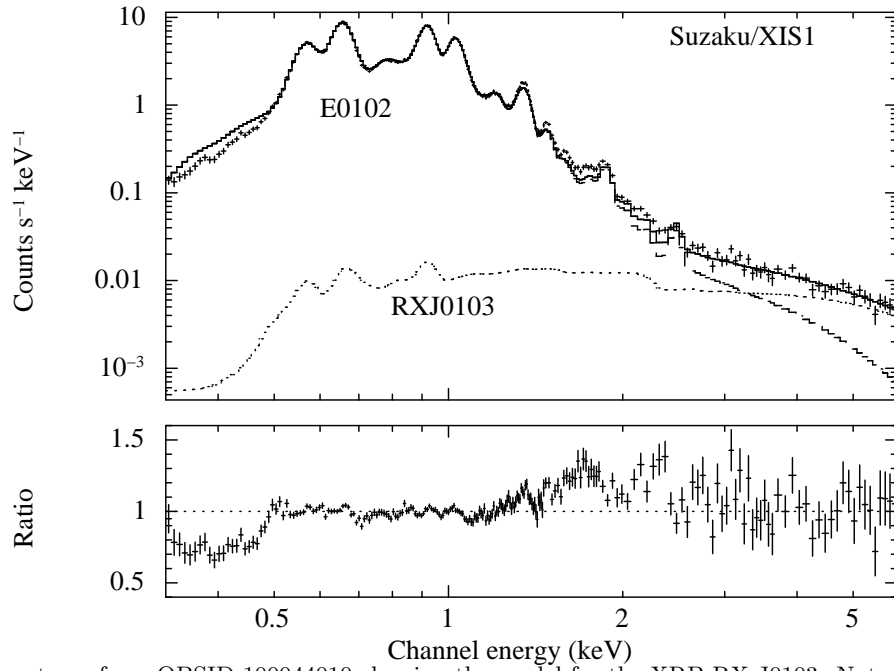


Figure 10. XIS1 spectrum from OBSID 100044010 showing the model for the XRB RX J0103. Note the residuals below 0.5 keV and above 1.5 keV.

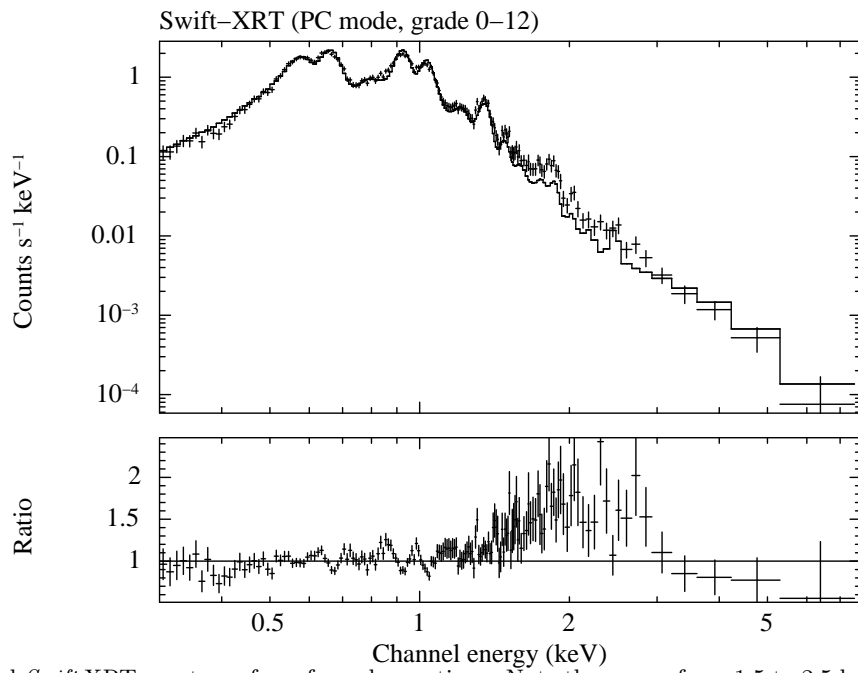


Figure 11. Combined *Swift* XRT spectrum from four observations. Note the excess from 1.5 to 2.5 keV, this is a signature of pileup.

REFERENCES

- [1] Weisskopf, M. C., Tananbaum, H. D., Van Speybroeck, L. P., and O'Dell, S. L., "Chandra x-ray observatory (cxo): overview," in [*X-Ray Optics, Instruments, and Missions III*], Truemper, J. E. and Aschenbach, B., eds., *Proc. SPIE* **4012**, 2 (2000).
- [2] Weisskopf, M. C., Brinkman, B., Canizares, C., Garmire, G., Murray, S., and Van Speybroeck, L. P., "An overview of the performance and scientific results from the chandra x-ray observatory," *Publications of the Astronomical Society of the Pacific* **114**, 1 (jan 2002).
- [3] Jansen, F., Lumb, D., Altieri, B., Clavel, J., Ehle, M., Erd, C., Gabriel, C., Guainazzi, M., Gondoin, P., Much, R., Munoz, R., Santos, M., Schartel, N., Texier, D., and Vacanti, G., "XMM-Newton observatory. I. The spacecraft and operations," *A&A*, **365**, L1–L6 (Jan. 2001).
- [4] Bautz, M., Pivovarov, M., Baganoff, F., Isobe, T., Jones, S., Kissel, S., Lamarr, B., Manning, H., Prigozhin, G., Ricker, G., Nousek, J., Grant, C., Nishikida, K., Scholze, F., Thornagel, R., and Ulm, G., "X-ray ccd calibration for the axaf ccd imaging spectrometer," in [*X-Ray Optics, Instruments, and Missions*], Hoover, R. B. and II, A. B. W., eds., *Proc. SPIE* **3444**, 210 (1998).
- [5] Garmire, G. P., Bautz, M. W., Ford, P. G., Nousek, J. A., and Ricker, G. R., "Advanced CCD imaging spectrometer (ACIS) instrument on the Chandra X-ray Observatory," in [*X-Ray and Gamma-Ray Telescopes and Instruments for Astronomy*], Truemper, J. and Tananbaum, H., eds., *Proc. SPIE* **4851**, 28–44 (Mar. 2003).
- [6] Garmire, G., Ricker, G., Bautz, M., Burke, B., Burrows, D., Collins, S., Doty, J., Gendreau, K., Lumb, D., and Nousek, J., "The axaf ccd imaging spectrometer," in [*American Institute of Aeronautics and Astronautics Conference*], 8 (1992).
- [7] den Herder, J. W., Brinkman, A. C., Kahn, S. M., Branduardi-Raymont, G., Thomsen, K., Aarts, H., Audard, M., Bixler, J. V., den Boggende, A. J., Cottam, J., Decker, T., Dubbeldam, L., Erd, C., Goulooze, H., Güdel, M., Guttridge, P., Hailey, C. J., Janabi, K. A., Kaastra, J. S., de Korte, P. A. J., van Leeuwen, B. J., Mauche, C., McCalden, A. J., Mewe, R., Naber, A., Paerels, F. B., Peterson, J. R., Rasmussen, A. P., Rees, K., Sakelliou, I., Sako, M., Spodek, J., Stern, M., Tamura, T., Tandy, J., de Vries, C. P., Welch, S., and Zehnder, A., "The Reflection Grating Spectrometer on board XMM-Newton," *A&A*, **365**, L7–L17 (Jan. 2001).
- [8] Turner, M. J. L., Abbey, A., Arnaud, M., Balasini, M., Barbera, M., Belsole, E., Bennie, P. J., Bernard, J. P., Bignami, G. F., Boer, M., Briel, U., Butler, I., Cara, C., Chabaud, C., Cole, R., Collura, A., Conte, M., Cros, A., Denby, M., Dhez, P., Di Coco, G., Dowson, J., Ferrando, P., Ghizzardi, S., Gianotti, F., Goodall, C. V., Gretton, L., Griffiths, R. G., Hainaut, O., Hochedez, J. F., Holland, A. D., Jourdain, E., Kendziorra, E., Lagostina, A., Laine, R., La Palombara, N., Lortholary, M., Lumb, D., Marty, P., Molendi, S., Pigot, C., Poindron, E., Pounds, K. A., Reeves, J. N., Reppin, C., Rothenflug, R., Salvétat, P., Sauvageot, J. L., Schmitt, D., Sembay, S., Short, A. D. T., Spragg, J., Stephen, J., Strüder, L., Tiengo, A., Trifoglio, M., Trümper, J., Vercellone, S., Vigroux, L., Villa, G., Ward, M. J., Whitehead, S., and Zonca, E., "The European Photon Imaging Camera on XMM-Newton: The MOS cameras," *A&A*, **365**, L27–L35 (Jan. 2001).
- [9] Strüder, L., Briel, U., Dennerl, K., Hartmann, R., Kendziorra, E., Meidinger, N., Pfeffermann, E., Reppin, C., Aschenbach, B., Bornemann, W., Bräuninger, H., Burkert, W., Elender, M., Freyberg, M., Haberl, F., Hartner, G., Heuschmann, F., Hippmann, H., Kastelic, E., Kemmer, S., Kettenring, G., Kink, W., Krause, N., Müller, S., Oppitz, A., Pietsch, W., Popp, M., Predehl, P., Read, A., Stephan, K. H., Stötter, D., Trümper, J., Holl, P., Kemmer, J., Soltau, H., Stötter, R., Weber, U., Weichert, U., von Zanthier, C., Carathanassis, D., Lutz, G., Richter, R. H., Solc, P., Böttcher, H., Kuster, M., Staubert, R., Abbey, A., Holland, A., Turner, M., Balasini, M., Bignami, G. F., La Palombara, N., Villa, G., Buttler, W., Gianini, F., Lainé, R., Lumb, D., and Dhez, P., "The European Photon Imaging Camera on XMM-Newton: The pn-CCD camera," *A&A*, **365**, L18–L26 (Jan. 2001).
- [10] Burrows, D. N., Hill, J. E., Nousek, J. A., Kennea, J. A., Wells, A., Osborne, J. P., Abbey, A. F., Beardmore, A., Mukerjee, K., Short, A. D. T., Chincarini, G., Campana, S., Citterio, O., Moretti, A., Pagani, C., Tagliaferri, G., Giommi, P., Capalbi, M., Tamburelli, F., Angelini, L., Cusumano, G., Brauning, H. W., Burkert, W., and Hartner, G. D., "The Swift X-Ray Telescope," *Space Science Reviews* **120**, 165–195 (2005).

- [11] Godet, O., Beardmore, A. P., Abbey, A. F., Osborne, J. P., Page, K. L., Tyler, L., Burrows, D. N., Evans, P., Starling, R., Wells, A. A., Angelini, L., Campana, S., Chincarini, G., Citterio, O., Cusamano, G., Giommi, P., Hill, J. E., Kennea, J., LaParola, V., Mangano, V., Mineo, T., Moretti, A., Nousek, J. A., Pagani, C., Perri, M., Capalbi, M., Romano, P., Tagliaferri, G., and Tamburelli, F., “The in-flight spectroscopic performance of the Swift XRT CCD camera during 2006-2007,” in [*UV, X-Ray, and Gamma-Ray Space Instrumentation for Astronomy XV. Edited by Siegmund, Oswald H. Proceedings of the SPIE, Volume 6686, pp. 66860A-66860A-8 (2007).*], Presented at the Society of Photo-Optical Instrumentation Engineers (SPIE) Conference **6686** (Sept. 2007).
- [12] Seward, F. D. and Mitchell, M., “X-ray survey of the Small Magellanic Cloud,” *ApJ*, **243**, 736–743 (Feb. 1981).
- [13] Gaetz, T. J., Butt, Y. M., Edgar, R. J., Eriksen, K. A., Plucinsky, P. P., Schlegel, E. M., and Smith, R. K., “Chandra X-Ray Observatory Arcsecond Imaging of the Young, Oxygen-rich Supernova Remnant 1E 0102.2-7219,” *ApJL*, **534**, L47–L50 (May 2000).
- [14] Hughes, J. P., Rakowski, C. E., and Decourchelle, A., “Electron Heating and Cosmic Rays at a Supernova Shock from Chandra X-Ray Observations of 1E 0102.2-7219,” *ApJL* **543**, L61–L65 (Nov. 2000).
- [15] Sasaki, M., Stadlbauer, T. F. X., Haberl, F., Filipović, M. D., and Bennie, P. J., “XMM-Newton EPIC observation of SMC SNR 0102-72.3 EPIC Observation of SMC SNR 0102-72.3,” *A&A* **365**, L237–L241 (Jan. 2001).
- [16] Flanagan, K. A., Canizares, C. R., Dewey, D., Houck, J. C., Fredericks, A. C., Schattner, M. L., Markert, T. H., and Davis, D. S., “Chandra High-Resolution X-Ray Spectrum of Supernova Remnant 1E 0102.2-7219,” *ApJ* **605**, 230–246 (Apr. 2004).
- [17] Rasmussen, A. P., Behar, E., Kahn, S. M., den Herder, J. W., and van der Heyden, K., “The x-ray spectrum of the supernova remnant 1e 0102.2-7219,” *A&A*, **365**, L231 (2001).
- [18] Wilms, J., Allen, A., and McCray, R., “On the Absorption of X-Rays in the Interstellar Medium,” *ApJ* **542**, 914–924 (Oct. 2000).
- [19] Russell, S. C. and Bessell, M. S., “Abundances of the heavy elements in the Magellanic Clouds. I - Metal abundances of F-type supergiants,” *ApJS* **70**, 865–898 (Aug. 1989).
- [20] Russell, S. C. and Dopita, M. A., “Abundances of the heavy elements in the Magellanic Clouds. II - H II regions and supernova remnants,” *ApJS* **74**, 93–128 (Sept. 1990).
- [21] Russell, S. C. and Dopita, M. A., “Abundances of the heavy elements in the Magellanic Clouds. III - Interpretation of results,” *ApJ* **384**, 508–522 (Jan. 1992).
- [22] Smith, R. K., Brickhouse, N. S., Liedahl, D. A., and Raymond, J. C., “Collisional Plasma Models with APEC/APED: Emission-Line Diagnostics of Hydrogen-like and Helium-like Ions,” *ApJL* **556**, L91–L95 (Aug. 2001).
- [23] Smith, R. and Brickhouse, N., “ATOMDB version 1.3.1,” <http://cxc.harvard.edu/atomdb/> (2006).
- [24] Dewey, D., “Extended Source Analysis for Grating Spectrometers,” in [*High Resolution X-ray Spectroscopy with XMM-Newton and Chandra*], Branduardi-Raymont, G., ed. (Dec. 2002).
- [25] Plucinsky, P. P., Schulz, N. S., Marshall, H. L., Grant, C. E., Chartas, G., Sanwal, D., Teter, M., Vikhlinin, A. A., Edgar, R. J., Wise, M. W., Allen, G. E., Virani, S. N., DePasquale, J. M., and Raley, M. T., “Flight spectral response of the ACIS instrument,” in [*X-Ray and Gamma-Ray Telescopes and Instruments for Astronomy. Edited by Joachim E. Truemper, Harvey D. Tananbaum. Proceedings of the SPIE, Volume 4851, pp. 89-100 (2003).*], Truemper, J. E. and Tananbaum, H. D., eds., 89–100 (Mar. 2003).
- [26] Marshall, H. L., Tennant, A., Grant, C. E., Hitchcock, A. P., O’Dell, S. L., and Plucinsky, P. P., “Composition of the Chandra ACIS contaminant,” in [*X-Ray and Gamma-Ray Instrumentation for Astronomy XIII. Edited by Flanagan, Kathryn A.; Siegmund, Oswald H. W. Proceedings of the SPIE, Volume 5165, pp. 497-508 (2004).*], Flanagan, K. A. and Siegmund, O. H. W., eds., 497–508 (Feb. 2004).
- [27] DePasquale, J. M., Plucinsky, P. P., Vikhlinin, A. A., Marshall, H. L., Schulz, N. S., and Edgar, R. J., “Verifying the ACIS contamination model with 1E0102.2-7219,” in [*Optical and Infrared Detectors for Astronomy. Edited by Garnett, James D.; Beletic, James W. Proceedings of the SPIE, Volume 5501, pp. 328-338 (2004).*], Holland, A. D., ed., 328–338 (Sept. 2004).
- [28] Haberl, F. and Pietsch, W., “Discovery of 1323 s pulsations from RX J0103.6-7201: The longest period X-ray pulsar in the SMC,” *A&A*, **438**, 211–218 (July 2005).